

Dynamical implications of sample shape for avalanches in 2-dimensional random-field Ising model with saw-tooth domain wall

Bosiljka Tadić

Department for Theoretical Physics; Jožef Stefan Institute; P.O. Box 3000; SI-1001 Ljubljana; Slovenia

We study dynamics of a built-in domain wall (DW) in 2-dimensional disordered ferromagnets with different sample shapes using random-field Ising model on a square lattice rotated by 45 degrees. The saw-tooth DW of the length L_x is created along one side and swept through the sample by slow ramping of the external field until the complete magnetisation reversal and the wall annihilation at the open top boundary at a distance L_y . By fixing the number of spins $N = L_x \times L_y = 10^6$ and the random-field distribution at a value above the critical disorder, we vary the ratio of the DW length to the annihilation distance in the range $L_x/L_y \in [1/16, 16]$. The periodic boundary conditions are applied in the y-direction so that these ratios comprise different samples, i.e., surfaces of cylinders with the changing perimeter L_x and height L_y . We analyse the avalanches of the DW slips between following field updates, and the multifractal structure of the magnetisation fluctuation time series. Our main findings are that the domain-wall lengths materialised in different sample shapes have an impact on the dynamics at all scales. Moreover, the domain-wall motion at the beginning of the hysteresis loop (HLB) probes the disorder effects resulting in the fluctuations that are significantly different from the large avalanches in the central part of the loop (HLC), where the strong fields dominate. Specifically, the fluctuations in HLB exhibit a wide multi-fractal spectrum, which shifts towards higher values of the exponents when the DW length is reduced. The distributions of the avalanches in this segments of the loops obey power-law decay and the exponential cutoffs with the exponents firmly in the mean-field universality class for long DW. In contrast, the avalanches in the HLC obey Tsallis density distribution with the power-law tails which indicate the new categories of the scale invariant behaviour for different ratios L_x/L_y . The large fluctuations in the HLC, on the other hand, have a rather narrow spectrum which is less sensitive to the length of the wall. These findings shed light to the dynamical criticality of the random-field Ising model at its lower critical dimension; they can be relevant to applications of the dynamics of injected domain walls in two-dimensional nanowires and ferromagnetic films.

I. INTRODUCTION

Controlled injection and motion of domain walls in planar magnetic wires and ferroic nanowires are of a renewed interest for the applications in new memory devices and domain-wall logic [1–3]. Techniques to inject a domain wall have been developed in technologically interesting materials as ferromagnetic films [4] and planar Permalloy nanowires [5–7] as well as in ferroelectric thin films [3, 8]. The motion of the wall in these systems results from an interplay between the applied external field and pinning at intrinsic defects and the morphology of the sample boundary. Some results indicate that the shape of the sample becomes increasingly relevant with the reduced dimensionality [9]. Moreover, the new visualisation techniques provide a direct observation of the domain-wall motion in different experimental settings [4, 10–15]; these experiments disclose important details of the stochastic dynamics and avalanching behaviour. For instance, the studies in [4, 11] reveal the domain-evolution patterns in ferromagnetic MnAs and Co films using time-resolved magneto-optical microscopy. The observed avalanches of domain-wall slips near the coercive field obey the scale invariance with tuneable scaling exponents, which depend on the position of the present domain wall concerning the underlying lattice, varied by changing temperature. In this context, theoretical investigations can provide additional information about the nature of the underlying stochastic processes of magnetisation reversal in two-dimensional disordered ferromagnets and narrow stripes with a built-in domain wall.

Disordered ferromagnetic films exhibiting criticality at the hysteresis loop [4, 11, 16–18] are conveniently modeled by two-dimensional random-field Ising model (2D-RFIM) [19–21], as described in Section II. Besides, these model systems are also of high importance for theoretical considerations for the following reasons. First, given that $d = 2$ appears to be the lower critical dimension of RFIM [22], there are no equilibrium phase transitions in 2D-RFIM (see a more detailed discussion in [20]). However, the non-equilibrium 2D-RFIM has a rich critical behaviour at the hysteresis loop with scale-invariance of the Barkhausen avalanches, as recently demonstrated by the extensive simulations in [19, 20]. Furthermore, compared to often studied three-dimensional model [23–25], the avalanching dynamics in 2D-RFIM appear to be more sensitive to the effects of the strength of the random-field disorder [19, 21], the presence of nonmagnetic defects [26], and for boundary conditions [27]. For instance, the finite-size scaling analysis using a vast span of system sizes [19, 21] revealed that the probability of spanning avalanches vanishes at a rather small critical disorder $R_c = 0.54 \pm 0.06$, compared to $R_c = 2.16$ in the three-dimensional model. Recently, the multi-fractal analysis of Barkhausen noise in 3D-RFIM demonstrated [28] a broad range of temporal scales in the magnetisation reversal processes. Although a non-trivial fractal structure can be expected for the Barkhausen noise in the 2D-RFIM, a detailed theoretical study is still missing.

In this work, we study the dynamics of a built-in domain wall in 2D-RFIM on a square lattice rotated by 45°; in this configuration, as shown in the Inset to Figure 1, the saw-

tooth wall which is prepared along the sample boundary of the length L_x can be moved by an infinitesimal change in the field when the disorder is absent. Therefore, by slowly ramping the external field along the descending branch of the hysteresis loop, the motion of the domain-wall at the beginning of the loop probes the true effects of the random-field disorder. Applying the multifractal analysis to filter the magnetisation reversal fluctuations at different scales, we distinguish the fluctuations at the beginning of the hysteresis loop from the processes at larger fields, i.e., the large-avalanches near the coercive field in the central part of the loop and the loop end. By fixing the total number of spins $N = L_x \times L_y = 10^6$ and the disorder above the critical value, we vary the domain-wall length in different sample shapes, corresponding to the ratio $L_x/L_y \in [1/16, 16]$. In the following Sections, we examine the impact of these geometrical shapes to the multifractal features of the magnetisation fluctuations time series and the scale-invariance of the avalanches in different segments of the hysteresis loop.

II. SIMULATION SETTINGS WITH SAW-TOOTH DOMAIN WALL

The two-dimensional square lattice is rotated by 45 degrees, see Fig. 1, and the DW is created along the sample side in the x -direction as follows. The spins in the first row are set to $S_{1x} = -1$ while the rest of sites have $S_{ij} = +1$ excluding the top row, which represents an open boundary with $S_{ix} = 0$. The periodic boundary conditions are applied in the y -direction. The varying external field B then drives the DW through the sample. Starting from a large positive value B_{max} and slowly decreasing along the descending branch of the hysteresis loop, the field is changed with a small rate $r \equiv \Delta B/J_0 = 10^{-3}$. The spin dynamics is governed by the interaction Hamiltonian Eq. (1), as described below. The spin flips next to the wall represent the DW motion to a new energetically stable position; the number of spin flips between two consecutive stable positions of the DW define an avalanche, cf. snapshots in Fig. 2. A quasi-static driving is applied, which means that the field is kept fixed during the avalanche propagation and then decreased again. The DW annihilates at the open top boundary.

The ferromagnetic spin-spin interaction in the presence of the random-field defects h_i at lattice sites $i = 1, 2, \dots, N$ and the time-varying external field $B(t)$ is given by the Hamiltonian

$$-\mathcal{H} = \sum_{i,j} J_{ij} S_i(t) S_j(t) + \sum_i h_i + B(t) \equiv + \sum_i h_i^{loc}(t) S_i(t), \quad (1)$$

where $J_{ij} = J_0 > 0$ for all pairs of the neighbouring spins. According to the second expression, the value of the local field $h_i^{loc}(t)$ experienced by a spin $S_i(t)$ at the site i and time t depends on the actual values of the near-neighbour spins, the quenched random field h_i at location i and the current value of the external field $B(t)$. As usual in the study of Barkhausen avalanches by RFIM [19–21, 23, 24, 26, 27], it suffices to consider the zero-temperature dynamics where the fields flip to align with the sign of the local field to minimise the energy,

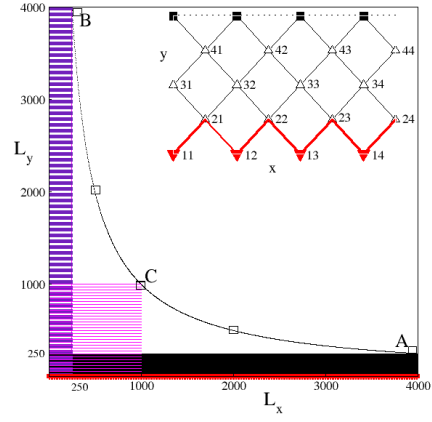


FIG. 1: Inset: Schematic presentation of the lattice with a saw-tooth domain wall (red line). The system is prepared with spin-down along the first row in x -direction and spin-up in the rest of sites until the top row, which is an open boundary (contains no spins). Periodic boundary conditions are applied in the transverse direction such that the left boundary in y -direction matches the right boundary, for instance, the site 31 matches 34, 44 matches 41 and so on, forming a cylindrical shape. The main figure depicts three shapes used in the simulations, termed A, B and C, which preserve the volume of $N = 10^6$ spins. The domain wall is always prepared along the L_x side.

i.e.,

$$S_i(t+1) = \text{sign} \left(h_i^{loc}(t) \right). \quad (2)$$

Also, a quenched random field h_i is taken from Gaussian distribution $h_i \in P(h, f)$ with a zero mean and the variance f (in units of J_0^2). In the simulations, we perform parallel updates of the whole system. That is, the local fields are computed at each site and kept until all spins are updated, which comprises one time step t of the simulations. Then the fields are calculated again, and the process is repeated until no spins are found that are not aligned with their current local fields. This step comprises the end of an avalanche, after which the external field is changed again, and so on.

Note that for the considered configuration, cf. Fig 1, in the absence of random fields, the spins at the second row can flip under an infinitesimally small energy. Thus, in the absence of disorder, the hysteresis loop is infinitely narrow and broadens according to the width of the distribution of the random fields. Therefore, this setting is suitable to test the actual impact of the random-field disorder to the avalanches in 2D-RFIM. In Fig. 2, we show snapshots of the domain-wall position in four samples with different strength of disorder. For a weak disorder, the DW accelerates with the changes in the external field, and eventually, DW depinning occurs in the middle of the hysteresis loop, resulting in a system-size avalanche. A precise analysis of the spanning avalanches in 2D-RFIM (but without built-in DW) was done in [21]; the finite-size scaling analysis revealed that the spanning avalanches could occur below a critical disorder $f_c^0 = 0.54 \pm 0.06$. In the presence of the extended DW, the finite-size scaling analysis performed in [27] suggests that the spanning avalanches can happen for a bit

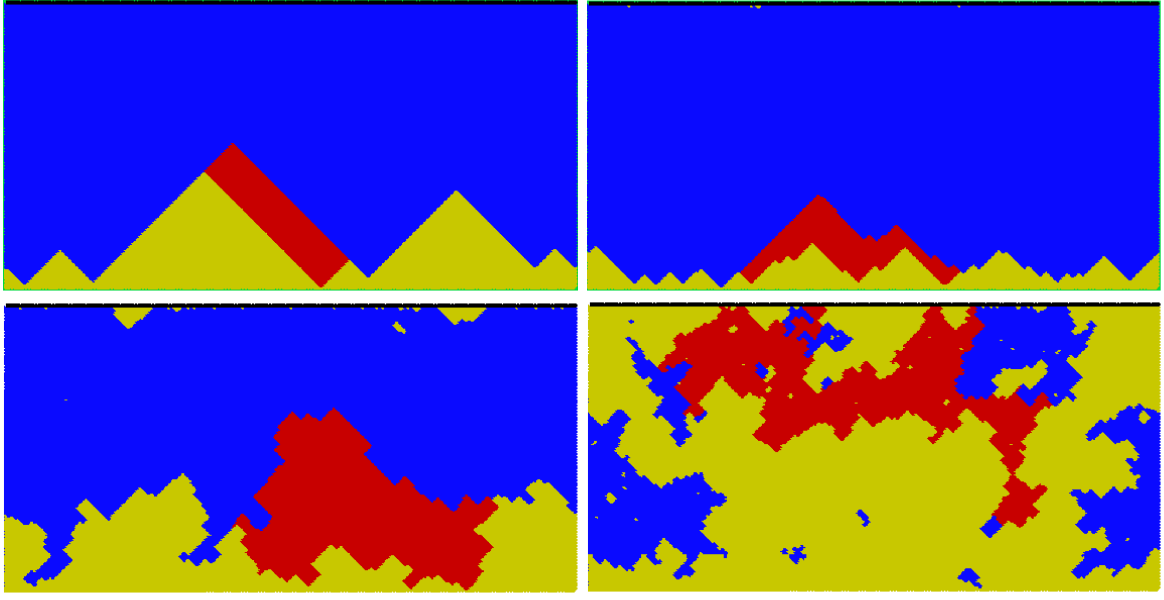


FIG. 2: Snapshots of the DW position (yellow) with the most recent avalanche (red) and the unflipped segments of the sample (blue). Different pictures correspond to the disorder strength below critical (top left), at the critical (top right) and two examples of disorder above the critical where the DW depinning is not possible, moderate (bottom left) and strong disorder (bottom right).

higher values up to the critical disorder $f_c = 0.64 \pm 0.06$. In the snapshots in Fig. 2, the spin flips which comprise the most recent avalanche (red areas) indicate that the presence of the extended DW induces anisotropic avalanches. Notably, the flips along the wall are energetically more favourable than the flips away from the wall, resulting in the elongated avalanche shapes even in a moderately strong disorder above the critical value. In this work, we consider the region above the critical disorder where, besides the system-wide DW, other spanning avalanches are not possible. Thus, in all simulations, we fix the disorder by $f = 0.8$, corresponding to the snapshot in the lower left panel of Fig. 2.

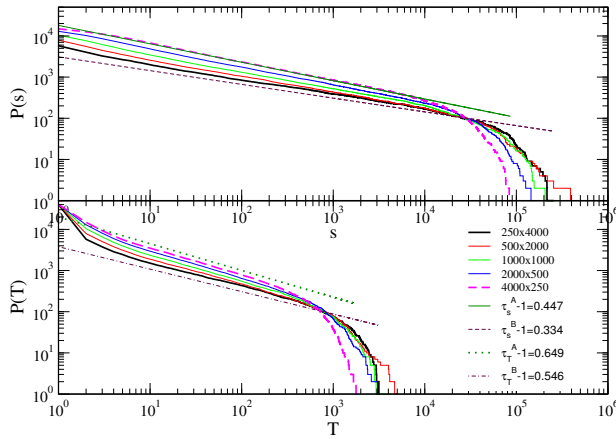


FIG. 3: Cumulative distributions of the avalanche size $P(s)$ and duration $P(T)$ for a fixed disorder $f = 0.8$ and varied volume-preserving shapes, indicated in the legend and in Fig. 1.

As above mentioned, the presence of the saw-tooth domain wall in the configuration shown in Fig. 1 provides a possibility to test the effects of the disorder, in particular, at the beginning of the hysteresis loop where the field is still weak and can not induce massive spin flips. Therefore the length of the DW is relevant for its motion by the same nominal disorder f . To explore the impact of the DW length, we fix the volume and change the sample shapes, as depicted in Fig. 1. The simulations are performed for five volume-preserving shapes indicated by small boxes along the hyperbolic curve in Fig. 1. The resulting distributions of the avalanche sizes and durations, integrated along the whole hysteresis branch, averaged over $10 \times$ realisations of random fields, are shown in Fig. 3. Notably, the sample shape affects the avalanches of magnetisation reversal. In particular, the scaling exponents are higher in the stripe with the long DW (sample-A) than in the samples with gradually shorter DW, see Table V. Eventually, in the stripe with the short DW (sample-B), we recover the exponents that are numerically close to those previously found [20] in the 2D-RFIM without a built-in DW. It is important to notice that the cut-offs of the distributions also vary with the DW length, suggesting that the long DW experiences different pinning effects than the short DW at the same nominal disorder. Moreover, these cut-offs differ from the usual exponential cutoffs.

Our analysis in the following two sections reveals that the origin of these avalanching behaviours is in the altered dynamics of the DW in different sample shapes. Following the dynamical analysis, we will show that various segments of the hysteresis loop contribute differently to the overall avalanching dynamics, depending on the length of the DW.

III. DYNAMICS OF THE MAGNETISATION REVERSAL IN DIFFERENT SEGMENTS OF THE HYSTERESIS LOOP

Following the statistics of the avalanches, mentioned above, a detailed inspection of the magnetisation reversal process from +1 to -1 shows the different course of the process in samples with different shapes, i.e., the length of DW. Here, we examine and compare these processes in three prototypal shapes indicated as A, B and C in Fig. 1. In particular, these are two narrow stripes (2D nano-wires) with the DW set along the longer side (sample A) and the shorter side (sample B), and the corresponding symmetrical shape with the same number of spins (sample C). The top panel of Fig. 4 shows how the magnetisation evolves with time in these samples. In particular, the reversal occurs in the shortest time in sample B having the short DW, while the evolution is slower in the shape A with the long DW, and the case of the symmetrical shape C is in between these two. Analogously, the hysteresis loop in the lower panel of Fig. 4 receives different forms; here, the long DW in the sample A results in the most slanted loop while the symmetrical and short DW cases lead to a more rectangular loop. Notice that the shape of the hysteresis loop near the coercive field, where the magnetisation eventually changes the sign, comprises of some large jumps (avalanches) of the magnetisation. While these large but finite jumps are in accord with the pinning by the supercritical disorder, they appear to vary with the sample shape, that is with lengths of the DW.

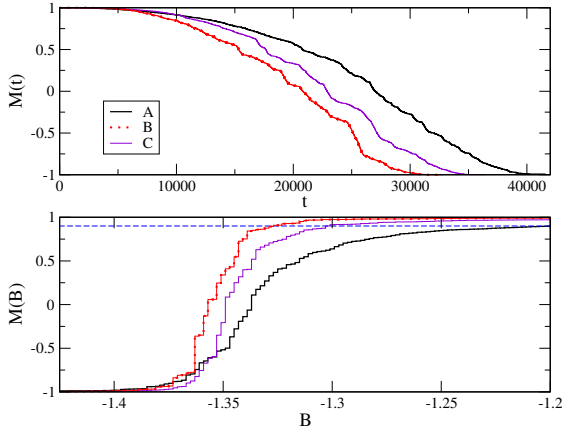


FIG. 4: Magnetisation as function of time (top) and the external field (bottom) for three samples marked as (A), (B) and (C), cf. Fig. 1.

Moreover, the fluctuations of the magnetisation along the hysteresis loop also differ with the varied shapes of the sample. For the samples A, B and C, in Fig. 5, we show the time series of the magnetisation changes $\delta M(t)$, which represents the number of reversed spins per time step t . In this type of signal, known as Barkhausen noise, an avalanche can be seen as a part of the signal above the baseline (level zero in this case). In agreement with the shape of the hysteresis loop in Fig. 4b, some large avalanches occur in the central part of the loop. They are most pronounced in sample B, which also features the fastest reversal. The large avalanches with gradually smaller sizes also occur in the central part of the loop in sam-

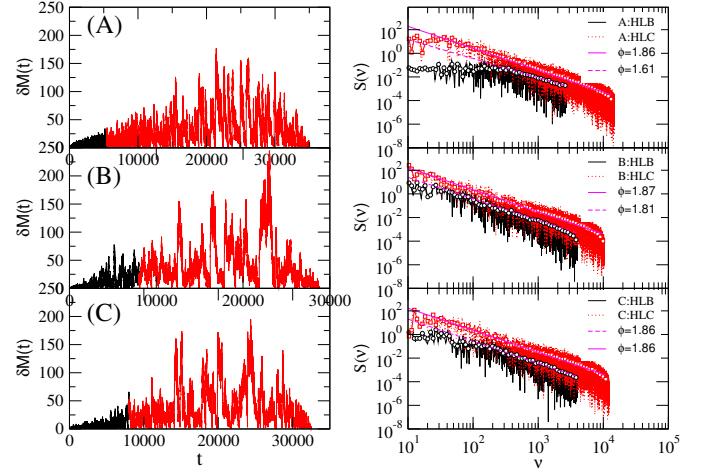


FIG. 5: The magnetisation fluctuation time series (left) and their power spectra (right) in samples marked as (A), (B) and (C), cf. Fig. 1. Black and red colour mark HLB and HLC segments of the hysteresis loop, respectively.

ple C and A, compatible with the extension of the respective reversal times. According to Fig. 4, the major differences occur at the beginning of the loop in different DW morphologies. Therefore, we consider the initial part of the signal, comprising of 5% of the total magnetisation reversal, as the hysteresis-loop-beginning (HLB) process, to be distinguished from the remaining signal, which is termed hysteresis-loop-central (HLC) process. In the following, we separately analyse the fluctuation features of these segments of the signal.

In the right panels of Fig. 5, we show the power spectra of these segments of the signal for sample shapes A, B and C. Notably, all signals exhibit temporal correlations, which are manifested in the power-law decay of the power spectrum as $S(v) \sim v^{-\phi}$ for a range of high frequencies v . The observed values of the exponent $\phi = 1.61 \pm 0.12$ in the HLB segment of sample A is the one that differs from $\phi = 1.84 \pm 0.06$ in the HLC. In the other two samples, the exponents are similar, and all are found in the range 1.80 – 1.90, probably dominated by the increasing trend of the signal with the increased field along the loop.

Further, we investigate the potential differences in these fluctuations at a wide range of scales, which can be filtered by multifractal analysis of the corresponding time series.

We apply the detrended multifractal analysis [28–32] of time series. The procedure utilises the underlying self-similarity, which is suitable for the analysis of Barkhausen noise signals [28]; it aims at exploring the scale invariance of the q -th order fluctuation function $F_q(n)$, defined below, which is expressed by a range of scaling exponents $H(q)$ (generalised Hurst exponent). Here, q is a real number taking a broad range of positive and negative values by which different segments of a multifractal time series get amplified such that they become self-similar to the rest of the signal. The standard procedure of the analysis consists of several steps [28, 30–32], in particular:

First, the profile of the time series $\delta M(k)$, $k = 1, 2, \dots, T_{max}$ is the time step index, is obtained by integration

$$Y(i) = \sum_{k=1}^i (\delta M(k) - \langle \delta M \rangle). \quad (3)$$

and divided into non-overlapping segments of equal length n . The process is repeated starting from the end of the time series; thus in total $2N_s = 2 \text{Int}(T_{max}/n)$ segments are considered for each time series. Then, the local trend $y_\mu(i)$ is determined (by non-linear interpolation) at each segment $\mu = 1, 2, \dots, N_s$, and the standard deviation around the local trend is computed:

$$F^2(\mu, n) = \frac{1}{n} \sum_{i=1}^n [Y((\mu-1)n+i) - y_\mu(i)]^2, \quad (4)$$

and similarly, $F^2(\mu, n) = \frac{1}{n} \sum_{i=1}^n [Y(N - (\mu - N_s)n + i) - y_\mu(i)]^2$ for $\mu = N_s + 1, \dots, 2N_s$. The q -th order fluctuation function $F_q(n)$ is then obtained for the segment length n and averaged over all segments.

$$F_q(n) = \left\{ (1/2N_s) \sum_{\mu=1}^{2N_s} [F^2(\mu, n)]^{q/2} \right\}^{1/q} \sim n^{H(q)}. \quad (5)$$

For a given q , the fluctuation function is plotted against varied segment length n and a scaling region (a straight line on double-log plot) examined to extract the corresponding Hurst exponent $H(q)$. The considered segment lengths vary in the range $n \in [2, \text{int}(T_{max}/4)]$. The distortion parameter q takes a range of real values, here $q \in [-6, +6]$, that allows to amplify *small fluctuation segments* by the negative values of q , and the segments with *large fluctuations*, for the positive values of q . Note that for $q = 2$, we obtain the well-known Hurst exponents of the standard deviation of the time series. Hence, if the time series is a monofractal, all values of the generalised Hurst exponent coincide and are equal (within the numerical error bars) to the standard Hurst exponent. In contrast, the multifractal time series exhibit different scaling exponents, that is, $H(q)$ is the function of q at least in a certain range of scales n , see the examples in Fig. 6. As discussed in the literature [29–32], the $H(q)$ dependence on q can be mapped to the singularity spectrum $\Psi(\alpha)$ of the time series via Legendre transform of $\tau(q)$, i.e., $\Psi(\alpha) = q\alpha - \tau(q)$, where $\alpha = d\tau/dq = H(q) + qdH/dq$. Here, $\tau(q)$ is the corresponding scaling exponent associated with the standard measure (box probability) in the partition function method.

As above mentioned, here we consider six different time series corresponding to the HLB and HLC in each of the three sample shapes A, B and C. In Fig. 6, we show the example of the fluctuation functions for the HLB and HLC part of the Barkhausen signal for sample A. This Figure shows that the fluctuation originating from the HLB scale differently than the fluctuations in the HLC. Appart from the wider multifractal spectrum in HLB, the values of the exponents $H(q)$ remain in the range below one, see the bottom panel in Fig. 6. This spectrum suggests that the profile is a fractional Brownian motion and, consequently, the original signal $\delta M(t)$, in this case,

is a fractional Gaussian noise. In contrast, the HLC fluctuations result with a more narrow spectrum with the exponents $H(q) > 1$, which is compatible with the sum of the fractional Brownian signals [28, 31]. The corresponding scaling exponents $H(q)$ for all considered sample shapes are shown in the bottom panel in Fig. 6. Noticeably, the enhanced small fluctuations (negative q -region of the spectra) are observed for HLB in all three sample shapes. The difference is that, for the sample B comprising of a short DW, the entire spectrum remains above the line $H = 1$. Whereas, in sample C with the symmetrical shape, the profile $H(q)$ for HLB fluctuations contains a mixture of the spectra seen in the samples A and B. In contrast, the spectra of the fluctuations in the HLC of all sample shapes are similar, cf. empty symbols in Fig. 6. We discuss these findings in the final Section V. In the following Section, we analyse these signals at a mesoscopic scale of avalanches occurring in the samples of different shapes.

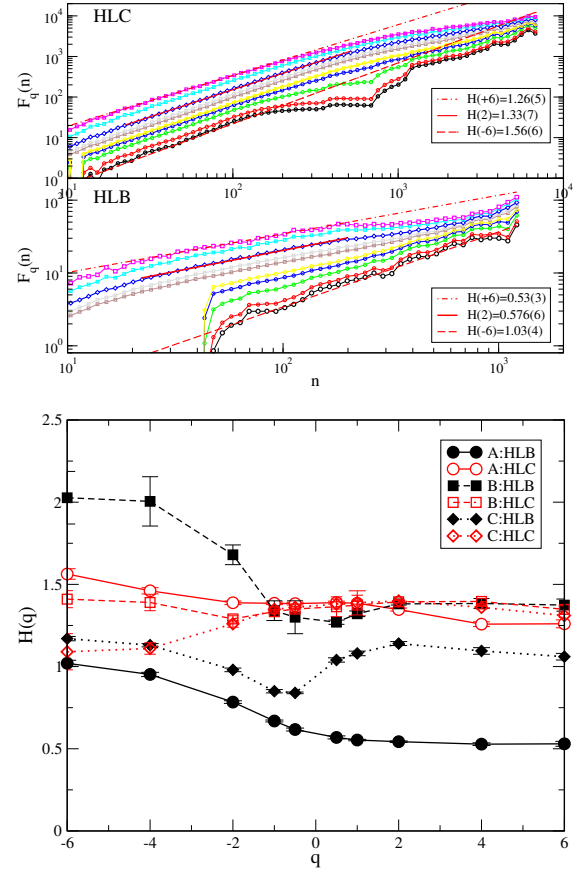


FIG. 6: Top panels: Fluctuation function $F_q(n)$ vs. interval length n for $q \in [-6, +6]$ bottom to top curves; two panels correspond to the signal originating from HLC and HLB segments of the hysteresis loop for sample A. Bottom panel: The generalised Hurst exponents $H(q)$ plotted against q for HLB and HLC fluctuations in all three samples A, B and C, as indicated in the legend.

IV. STATISTICS OF THE MAGNETISATION REVERSAL AVALANCHES IN DIFFERENT SAMPLE SHAPES

By definition, an avalanche represents a clustering of events along the time series; hence, it consists of a number of the elementary pulses. According to the dynamical analysis of the magnetisation fluctuations time series in Sec. III, we expect that the observed different stochastic processes have an impact to the avalanches. Specifically, we separate the contribution arising in the process at the beginning of the hysteresis loop, where the disorder is essential to the DW motion, from the processes in its centre, where the field is strong enough to induce maximal avalanches in a given DW configuration and the strength of disorder. From the simulations, we determine the avalanche distributions associated with the HLB and HLC for the considered sample shapes. The distributions are averaged over 10 random-field configurations. For each sample shape, the corresponding configurations of the random fields are generated starting from the same seed. The results depicted in Figs. 7, Fig. 8 and Fig. 9 are for the samples A, B and C, respectively.

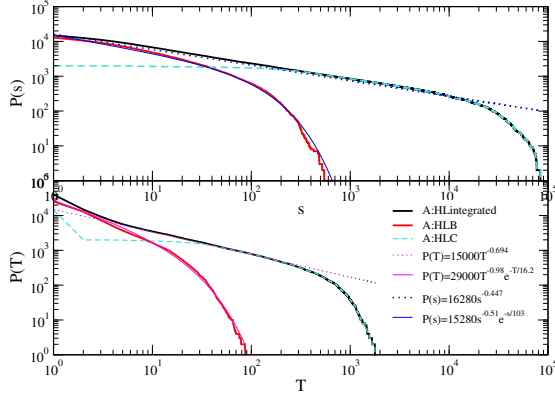


FIG. 7: Cumulative distributions of the avalanche size $P(s)$ and duration $P(T)$ for HLB (red line) and HLC segment (dashed magenta line) and the distribution integrated along the hysteresis branch (black line); the results are for the narrow stripe $L_x = 16L_y$ with a long DW (sample A).

In sample A, featuring the long DW, we find that the distribution of size $P(s)$ and duration $P(T)$ of the avalanches recorded in the initial part of the hysteresis loop can be fitted by power-law decay up to the exponential cut-off. Specifically, we have

$$P(T) = aT^{-(\tau_T-1)}e^{-T/T_0}, \quad (6)$$

for the avalanche duration T , and similarly for the avalanche size s , cf. legend in Fig. 7. The fitted values for the corresponding exponents $\tau_s - 1 = 0.51 \pm 0.04$, $\tau_T - 1 = 0.98 \pm 0.05$ indicate a familiar mean-field universality class for the HLB criticality. In contrast, the distributions integrated over the entire branch of the hysteresis loop exhibit a scale-invariance with different exponents and non-exponential cutoffs. In particular, the exponents are $\tau_s - 1 = 0.447$ and $\tau_T - 1 = 0.694$,

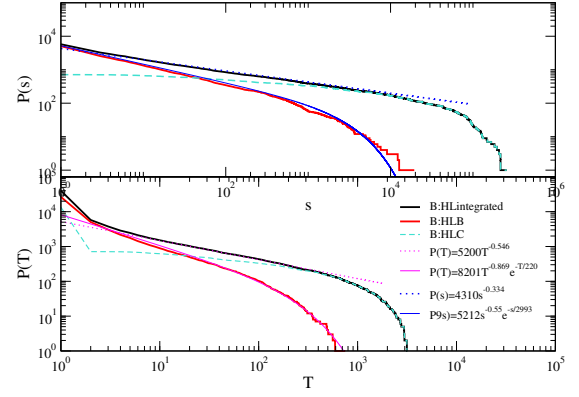


FIG. 8: Cumulative distributions of the avalanche size $P(s)$ and duration $P(T)$ for HLB (red line) and HLC segment (dashed magenta line) and the distribution integrated along the hysteresis branch (black line); the results are for the narrow stripe $L_x = L_y/16$ with a short DW (sample B).

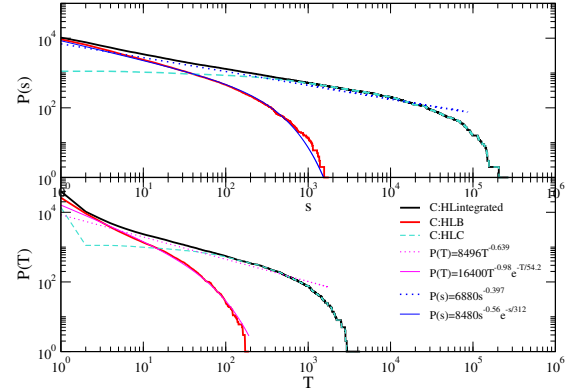


FIG. 9: Cumulative distributions of the avalanche size $P(s)$ and duration $P(T)$ for HLB (red line) and HLC segment (dashed magenta line) and the distribution integrated along the hysteresis branch (black line); the results are for the symmetrical sample $L_x = L_y$ (sample C).

within the numerical error-bars ± 0.009 , suggesting a new class of the avalanching dynamics. Importantly, in the scaling and cutoff region, these distributions coincide with the distributions obtained from the central part of the hysteresis loop (dashed line). Hence, the avalanching dynamics accompanying the motion of the long DW in the central part of the hysteresis loop is responsible for the new critical behaviour. A more detailed discussion is given in Section V.

The presence of the short DW in sample B manifests in somewhat different avalanche behaviour, as shown in Fig. 8. In particular, for the HLB, fits of the distributions by the expression (6) lead to the exponents $\tau_s = 0.551$ and $\tau_T - 1 = 0.869$, numerically close to the exponents obtained in [20] for the 2D-RFIM without any built-in DW. The loop-integrated distributions, in this case, lead to the exponents $\tau_s - 1 = 0.33$ and $\tau_T - 1 = 0.54$, deviating from the distribution in HLC, which are almost flat (see below). It is interesting to note that

these numerical values are close to the exact values $\tau_s = 4/3$ and $\tau_T = 3/2$ derived for the avalanches in the directed sandpile automata [33], representing the probability of a meeting of two random walks initiated at the same point. The simulations in the symmetrical sample, where the DW length is equal to the transverse distance L_y , confirm that the change of the exponents is indeed caused by the extension of the DW. The results for sample C are shown in Fig. 9, where the fits with the expression (6) give the mean-field exponents for HLB avalanches, and the corresponding exponents in the HLC and the loop-integrated distributions are in between the exponents in samples A and B.

To further explore the contribution of the dynamics from the central segments of the hysteresis loop to the occurrence of the new universality classes of avalanches of the DW slips, we determine and fit the *probability density* of the size and duration of these avalanches. The distributions for all sample shapes, averaged over $20\times$ realisations of random fields, are shown in Fig. 10.

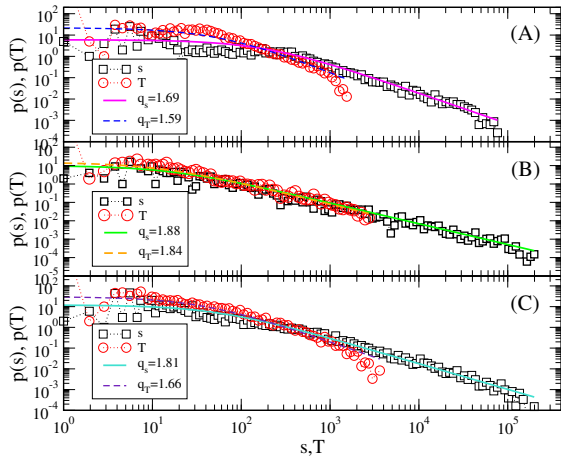


FIG. 10: Differential distributions of the avalanche size s and duration T in the central part of the hysteresis loop for three sample shapes A, B and C (data are log-binned). The fits according to Tsallis density function Eq. (7) with the indicated q_s and q_T values.

In contrast to the expression (6) that applies to the avalanche distributions in HLB, the differential distributions for the avalanche size s in HLC can be better fitted by Tsallis density function [34, 35]

$$p(s) = B_s [1 - (1 - q_s)s/s_0]^{-\frac{1}{1-q_s}}, \quad (7)$$

and similarly for the distribution of the duration T . For varied sample shapes, these distributions appear to have different slopes, i.e., nonextensivity parameters q_s and q_T , as indicated in the figure legends. Specifically, with the decrease of the ratio L_x/L_y the scaling exponent $\tau_s = 1/(q_s - 1)$ systematically decreases from 1.44 (in sample A) to 1.24 (sample C) to 1.13 (sample B). Hence, the exponent of the corresponding cumulative HLC distribution in Fig. 8 is close to zero within the numerical error bars (fitting the slope for sample B in Fig. 10 gives $\tau_s = 1.08 \pm 0.09$). It is interesting to compare these

geometrical effects on the DW-slip avalanches with the experimentally observed tuning of the scaling exponent τ_s in Ref. [4]. Considering the distribution of the duration of avalanches, we also find that the exponent $\tau_t = 1/(q_t - 1)$ varies from 1.69 (sample A) to 1.51 (sample C) and 1.19 (sample B). A possible origin of Tsallis distribution in the context of the domain-wall avalanches, and the observed different classes of criticality are also discussed in Section V.

V. DISCUSSION AND CONCLUSIONS

We have considered magnetisation reversal processes in a model of two-dimensional ferromagnet with the morphology that allows built-in saw-tooth DW of the length L_x along one side of the sample. By fixing the number of spins, we considered several sample shapes by varying the ratio L_x/L_y . Given the periodic boundaries along L_y boundary, the considered samples comprise of cylindrical shapes with a different diameter L_x . Simulating zero-temperature RFIM dynamics under slow field ramping, we have analysed the motion of the domain wall through the sample until it is annihilated at the open top boundary, comprising the complete magnetisation reversal along the hysteresis branch. Our analysis in this paper focuses on the fluctuations of magnetisation at different scales, which are filtered by the detrended multifractal analysis of the Barkhausen noise time series, and their impact to the avalanches of the domain-wall slips. Also, we fixed the strength of the random-field disorder $f = 0.8 > f_c$ that prevents the domain-wall depinning or the appearance of other (linear) spanning avalanches in the process. In the considered morphology, the avalanches always start from the domain-wall position (initially at the bottom boundary of the sample).

Our main findings are that different sample shapes (allowing different lengths of the domain wall) have implications for the magnetisation reversal noise at all scales from the elementary pulses to avalanches of the domain-wall slips. Moreover, the impact of the domain-wall length on its dynamics differs at the beginning of the hysteresis loop (HLB), where the disorder effects are dominant, from the remaining part of the hysteresis loop (HLC), corresponding to the stronger external field. Specifically, we find that

- the magnetisation fluctuations at the beginning of the hysteresis loop exhibit multifractal features with a broad spectrum; enhanced small changes occur in all sample shapes. However, the multifractal spectrum gradually shifts from the region of the fractional Gaussian noise (for large DW, sample A) to fractional Brownian motion fBM (in the case of short DW, sample B). For the processes with large avalanches in HLC, a narrow spectrum corresponding to fBM is found, which is less sensitive to the DW length.
- the scale-invariance of the avalanches in HLB belongs to the familiar mean-field universality class, in particular for a long DW. In sample with the short DW, the exponents are numerically close to those in 2D-RFIM without a built-in DW [20].

TABLE I: Scaling exponents τ_s and τ_T of the domain-wall slip avalanche size and duration in Figs. 7-9, determined in the beginning (HLB) part and integrated (HLI) along the hysteresis loop for different sample shapes indicated by A, B and C in Fig. 1. The numerical error bars are shown in scopes. The corresponding anisotropy exponent ζ , the fractal dimension $D_{||}$ and the dynamics exponent z are computed using the scaling relations, see text.

exp sample	A:HLB	A:HLI	B:HLB	B:HLI	C:HLB	C:HLI
τ_s	1.5(1)	1.44(7)	1.5(5)	1.33(4)	1.5(6)	1.39(7)
τ_T	1.9(8)	1.69(4)	1.86(9)	1.54(6)	1.9(8)	1.63(9)
ζ	0.92	0.55	0.61	0.62	0.75	0.60
$D_{ }$	1.92	1.55	1.61	1.62	1.75	1.60
z	1.84	1.11	1.22	1.23	1.51	1.21

- The avalanche distributions in HLB obey a commonly known power-law decay with the exponential cutoffs. In contrast, the avalanches in HLC follow Tsallis density distribution with the power-law tails. The corresponding scaling exponents are tuned by changing the ratio of the length of the DW to the transverse distance where the DW is annihilated. It is interesting to note that the range of the variation of the exponent τ_s , induced by these geometrical effects, coincides with the experimental results in [4], despite the absence of dipolar interactions. A summary of all scaling exponents is given in Table V.

The impact of the DW length for the scaling exponents of the avalanches can be related with effective long-range correlations of disorder along the DW in a low-dimensional geometry. Potentially, such a DW “elasticity” can also be seen as the origin of Tsallis distributions in HLC avalanches. In the literature, different universality classes of disorder-induced critical behaviour have been revealed [36, 37], corresponding to weak and strong disorder. The models with the long-range correlations of randomness (quenched and annealed) have been studied by the renormalization group (RG) methods in [38, 39]. In this context, the anisotropy induced by the built-in DW manifests itself in the dynamics and the avalanche geometry, leading to the following spatial scaling of the avalanche size

$s(x) = x_{||}^{D_{||}} \Phi(x_{\perp}/x_{||}^{\zeta})$. Here, ζ identifies the anisotropy exponent and $D_{||}$ is the fractal dimension of the avalanche in the direction parallel to the wall. Using the RG arguments [38] for the diffusion in the presence of anisotropic correlations of disorder, one can derive these exponents from the avalanche statistics, in particular, $D_{||} \equiv 1 + \zeta = \frac{\tau_T - 1}{\tau_s - 1}$ and, to leading order of RG, $z = 2\zeta$ [38]. The numerical values of the derived exponents are also listed in Table V, subject to the statistical error bars of the avalanche distributions. The largest difference in the anisotropy exponent at HLB and HLC occurs in sample A with the long DW. The difference is reduced in the symmetrical shape, sample C, while it practically vanishes in sample B with the small DW. A similar observation extends to the dynamical exponents z , cf. Table V. The two values of z for sample A once again confirm the conclusions of two different types of stochastic processes occurring in HLB and HLC, suggested by the multifractal analysis in Section III.

In summary, our study of the dynamics of injected DW in low-dimensional ferromagnets driven by the external field reveals its multifractal features and the dependence on the sample shapes, which can be relevant for practical applications, e.g., to design on the DW-based memory devices. Furthermore, these observations shed light to the dynamic criticality of the RFIM at its lower critical dimension. The observed dynamic critical behaviours reveal sensitivity to the boundary conditions, sample shapes and the DW length. These conclusions are derived from numerical simulations for moderately high random field pinning above the critical disorder. The case of the weak disorder is left for future work as well as further theoretical analysis by RG approaches, which can precisely identify the potential universality classes.

Acknowledgments

The author acknowledges the financial support from the Slovenian Research Agency (research code fund- ing number P1-0044).

-
- | | |
|---|--|
| <p>[1] D.A. Allwood, G. Xiong, C.C. Fulkner, D. Atkinson, D. Petit, and R.P. Cowbrun. Magnetic domain-wall logic. <i>Science</i>, 309, 2005.</p> <p>[2] S.S.P. Parkin, M. Hayashi, and L. Thomas. Magnetic domain-wall racetrack memory. <i>Science</i>, 320, 2008.</p> <p>[3] J.R. Whyte and J.M. Gregg. A diode for ferroelectric domain-wall motion. <i>Nature Communications</i>, 6, 2015.</p> <p>[4] S-C. Shin, K-S. Ryu, D-H. Kim, and H. Akinaga. Two-dimensional critical scaling behavior of barkhausen avalanches (invited). <i>Journal of Applied Physics</i>, 103:07D907, 2008.</p> <p>[5] R.P. Cowbrun, D.A. Allwood, G. Xiong, and M.D. Cooke. Domain wall injection and propagation in planar permalloy nanowires. <i>J. Appl. Phys.</i>, 91, 2002.</p> <p>[6] S. Savel’ev, A. Rakhmanov, and F. Nori. Experimentally realizable devices for domain wall motion control. <i>New J. Phys.</i>, 7,</p> | <p>2005.</p> <p>[7] T. Phung, A. Pusp, and L. et al Thomas. Highly efficient in-line magnetic domain wall injector. <i>Nano Letters</i>, 15, 2015.</p> <p>[8] I.J. McGilly, P. Yudin, I. Feigl, A.K. Tagantsev, and N. Setter. Controlling domain wall motion in ferroelectric thin films. <i>Nature Nanotechnol.</i>, 10, 2015.</p> <p>[9] C. Garg, S-H. Yang, T. Phung, A. Pushp, and S. Parkin. Dramatic influence of curvature of nanowire on chiral domain wall velocity. <i>Science Adv.</i>, 3, 2017.</p> <p>[10] A. Schwarz, M. Liebmann, U.Kaiser, R. Wiesendanger, T-W. Noh, and D-W. Kim. Visualization of the barkhausen effect by magnetic force microscopy. <i>Phys. Rev. Lett.</i>, 92:077206, Feb 2004.</p> <p>[11] K-S. Ryu, H. Akinaga, and S-C. Shin. Tunable scaling behaviour observed in barkhausen criticality of a ferromagnetic</p> |
|---|--|

- film. *Nat. Phys.*, 3, 2007.
- [12] X. Jiang, L. Thomas, R. Moriya, M. Hayashi, B. Bergman, C. Rettner, and S.S.P. Parkin. Enhanced stochasticity of domain wall motion in magnetic racetracks due to dynamic pinning. *Nat. Commun.*, 1:25, 2010.
- [13] A. Singh, S. Mukhopadhyay, and A. Ghosh. Tracking random walk of individual domain walls in cylindrical nanomagnets with resistance noise. *Phys. Rev. Lett.*, 105:067206, Aug 2010.
- [14] H-S. Lee, K-S. Ryu, C-Y. You, K-R. Jeon, S. S.P. Parkin, and S-C. Shin. Reduced stochasticity in domain wall motion with increasing pinning density in thin fe films. *New Journal of Physics*, 13(8):083038, 2011.
- [15] K-S. Ryu and S-C. Shin. Magnetic symmetry dependent wall domain motion mechanisms in two-dimensional ferromagnetic systems. *J. Applied Physics*, 121:013901, 2017.
- [16] E. Puppín. *Phys. Rev. Lett.*, 84, 2000.
- [17] H-S. Lee, K-S. Ryu, I-S. Kang, and S-C. Shin. Universal Barkhausen critical scaling behavior observed in $\text{Ni}_x\text{Fe}_{1-x}$ ($x=0-0.5$) films. *Journal of Applied Physics*, 109(7), 2011.
- [18] H-S. Lee, K-S. Ryu, C-Y. You, K-R. Jeon, S-H. Yang, S.S.P. Parkin, and S-C. Shin. Asymmetric magnetic disorder observed in thermally activated magnetization reversal of exchange-biased irmn/cofe films. *Journal of Magnetism and Magnetic Materials*, 325:13 – 16, 2013.
- [19] D. Spasojević, S. Janičević, and M. Knežević. Numerical evidence for critical behavior of the two-dimensional nonequilibrium zero-temperature random field ising model. *Phys. Rev. Lett.*, 106:175701, Apr 2011.
- [20] D. Spasojević, S. Janičević, and M. Knežević. Avalanche distributions in the two-dimensional nonequilibrium zero-temperature random field ising model. *Phys. Rev. E*, 84:051119, Nov 2011.
- [21] D. Spasojević, S. Janičević, and M. Knežević. Analysis of spanning avalanches in the two-dimensional nonequilibrium zero-temperature random-field ising model. *Phys. Rev. E*, 89:012118, Jan 2014.
- [22] M. Aizenman and J. Wehr. *Phys. Rev. Lett.*, 62:2503, 1989.
- [23] F. J. Pérez-Reche and E. Vives. Finite-size scaling analysis of the avalanches in the three-dimensional gaussian random-field ising model with metastable dynamics. *Phys. Rev. B*, 67:134421, Apr 2003.
- [24] F. J. Pérez-Reche and E. Vives. Spanning avalanches in the three-dimensional gaussian random-field ising model with metastable dynamics: Field dependence and geometrical properties. *Phys. Rev. B*, 70:214422, Dec 2004.
- [25] B. Tadić. Switching current noise and relaxation of ferroelectric domains. *The European Physical Journal B - Condensed Matter and Complex Systems*, 28(1):81–89, 2002.
- [26] B. Tadić. Nonuniversal scaling behavior of barkhausen noise. *Phys. Rev. Lett.*, 77:3843–3846, Oct 1996.
- [27] B. Tadić and U. Nowak. Barkhausen avalanches in anisotropic ferromagnets with 180° domain walls. *Phys. Rev. E*, 61:4610–4613, Apr 2000.
- [28] B. Tadić. Multifractal analysis of barkhausen noise reveals the dynamic nature of criticality at hysteresis loop. *Journal of Statistical Mechanics: Theory and Experiment*, 2016(6):063305, 2016.
- [29] A.N. Pavlov and V. S. Anishchenko. Multifractal analysis of complex signals. *Physics–Uspekhi*, 50:819–834, 2007.
- [30] J. W. Kantelhardt, S. A. Zschiegner, E. Koscielny-Bunde, S. Havlin, A. Bunde, and H.E. Stanley. Multifractal detrended fluctuation analysis of nonstationary time series. *Physica A: Statistical Mechanics and its Applications*, 316:87 – 114, 2002.
- [31] M. S. Movahed, G. R. Jafari, F. Ghasemi, S. Rahvar, and M. R. Rahimi Tabar. Multifractal detrended fluctuation analysis of sunspot time series. *Journal of Statistical Mechanics: Theory and Experiment*, 2006(02):P02003, 2006.
- [32] S. Drozd and P. Oswiecimka. Detecting and interpreting distortions in hierarchical organization of complex time series. *Phys. Rev. E*, 91:030902(R), 2015.
- [33] D. Dhar and R. Ramaswamy. *Phys. Rev. Lett.*, 1990.
- [34] C. Tsallis and M. Gell-Mann, editors. *Nonextensive entropy—interdisciplinary applications*. Oxford University Press, 2004.
- [35] G.P. Pavlos, L.P. Karakatsanis, M.N. Xenakis, E.G. Pavlos, A.C. Iliopoulos, and D.V. Sarafopoulos. Universality of non-extensive tsallis statistics and time series analysis: Theory and applications. *Physica A: Statistical Mechanics and its Applications*, 395:58 – 95, 2014.
- [36] M. Cieplak, A. Maritan, and J. R. Banavar. Optimal paths and domain walls in the strong disorder limit. *Phys. Rev. Lett.*, 72:2320–2323, Apr 1994.
- [37] B. Tadić. Dynamic criticality in driven disordered systems: role of depinning and driving rate in barkhausen noise. *Physica A: Statistical Mechanics and its Applications*, 270:125 – 134, 1999.
- [38] B. Tadić. Disorder-induced critical behavior in driven diffusive systems. *Phys. Rev. E*, 58:168–173, Jul 1998.
- [39] N.V. Antonov and P.I. Kakin. Effects of random environment on a self-organized critical system: Renormalization group analysis of a continuous model. *EPJ Web of Conferences*, 108:02009, 2016.